Coupling actin flow, adhesion, and morphology in a computational cell motility model

Danying Shao [*], **Herbert Levine** [*], **and Wouter-Jan Rappel** [*]

[*] Center for Theoretical Biological Physics and Department of Physics, University of California, San Diego, La Jolla, CA 92093-0374, USA

Submitted to Proceedings of the National Academy of Sciences of the United States of America

Cell migration is a pervasive process in many biology systems and involves protrusive forces generated by actin polymerization, myosin dependent contractile forces, and force transmission between the cell and the substrate through adhesion sites. Here we develop a computational model for cell motion that uses the phase field method to solve for the moving boundary with physical membrane properties. It includes a reaction-diffusion model for the actin-myosin machinery and discrete adhesion sites which can be in a "gripping" or "slipping" mode and integrates the adhesion dynamics with the dynamics of the actin filaments, modeled as a viscous network. To test this model, we apply it to fish keratocytes, fast moving cells that maintain their morphology, and show that we are able to reproduce recent experimental results on actin flow and stress patterns. Furthermore, we explore the phase diagram of cell motility by varying myosin II activity and adhesion strength. Our model suggests that the pattern of the actin flow inside the cell, the cell velocity and the cell morphology are determined by the integration of actin polymerization, myosin contraction, adhesion forces, and membrane forces.

cell migration | actin-myosin contraction | adhesion | phase field

introduction

Cell migration plays a crucial role in many biological processes, including chemotaxis, embryogenesis, and cancer metastasis. In eukaryotic cells, this migration is powered by the actin-myosin system [1]: at the cell's leading edge, cross-linked actin filaments polymerize by adding actin monomers to their barbed ends, a process known as "tread-milling", while at the back of the cell, myosin II, from now on referred to as myosin, binds to the bundled actin filaments and exerts contractile stress.

Recent experiments have examined cytosolic actin flow, the movement of actin network with respect to the substrate [2, 3, 4, 5, 6]. Many of these studies were performed using fish epidermal keratocytes. These cells are ideally suited to investigate cell motion since they are able to maintain a polarized morphology and display rapid migration on the substrate [7]. These studies revealed that in the front half of the cell, the actin network exhibits a small retrograde flow in the laboratory's frame of reference. In contrast, the trailing part of the cell displays anterograde actin flow at larger speed. This pattern of the actin flow, along with cell velocity and cell shape, was found to be dependent on various factors, including the rate of actin polymerization, the amount of myosin activity in the cell, and the cell-substrate adhesiveness [3, 8, 6].

The active stresses generated by the actin-myosin system are transmitted to the substrates through adhesion sites, providing the necessary forces required for propulsion [2, 9, 10]. These adhesion sites are formed near the front of the cell, grow into mature focal adhesions and gradually disassemble as the cell advances [10, 11, 12]. The force transmission between cells and the substrate is often viewed as a clutch that is either engaged or disengaged [13, 14, 15]. In the engaged, or gripping, mode the cell's cytoskeleton is firmly attached to the substrate while in the disengaged, or slipping, mode there is slippage between the cytoskeleton and the substrate. A recent experimental study using keratocytes examined the relationship between actin flow and substrate stress [2] and showed that the substrate stress vector was not aligned with the actin velocity vector in the central part of the cell. This study suggests that traction at the front of the cell is generated by adhesion sites that are in the gripping mode while traction in the sides and back is generated by sites in the slipping mode.

Even though experiments have generated numerous quantitative results, the precise mechanisms of cell motion remain poorly understood. A number of recent theoretical studies have attempted to model cell migration in an effort to probe the motility mechanism. Most of these models, however, make several simplifications and do not address the full coupling between adhesion sites, actin flow, and cell morphology. For example, some studies determined the actin flow in a one-dimensional [16, 17, 18] or fixed two-dimensional cell geometry [19]. In other studies, the cell boundary was allowed to change according to a phenomenal function of protrusion rate [6, 20] while other approaches implemented physical forces along the cell membrane, obtained cell shape and speed, but ignored actin flow and detailed adhesion mechanisms [21, 22, 23]. Other studies examined adhesion dynamics and cell-substrate coupling ignoring cell deformations [24, 25, 26] or focused on the dynamics of the leading edge [27, 28]. Finally, a recently developed computational technique is able to simulate migrating three-dimensional cells but does not include discrete adhesion sites [29].

In this study, we present a comprehensive model for cell migration which couples actin flow with discrete adhesion sites and deformable cell boundaries. These moving boundaries are solved, as in previous studies [22, 23], using the phase field method. This method is a computationally efficient method in which the physical membrane forces, including surface tension and bending energy, can be modeled without the explicit need of boundary tracking. In our model, cell motion is generated through myosin contraction and actin polymerization, which are both treated as active stresses [18]. In addition, we include discrete adhesion sites which can be either in the gripping or slipping mode and whose dynamics is integrated with actin flow. Even though our model is easily formulated for general eukaryotic cell motion, we will apply it to keratocyte motility and will show that it can accurately account for a number of experimental findings. Furthermore, we show that we can start exploring different experimental conditions through simple modifications of the parameters.

Model

Our model is motivated by experiments on keratocytes and considers cell shapes that reach a stationary state. A schematic side-view of a keratocyte cell is given in Fig. 1A and shows a bulb-shaped cell body and a thin lamellipodium. Since lamellar fragments can maintain typical fan-like shapes and motility [7] we will ignore this cell body and

Reserved for Publication Footnotes

will treat the lamellipodium as a two-dimensional object, shown as a top view in Fig. 1B.

Our model exists of four coupled "modules", each describing different aspects of cell motility. More details of our model can be found in the Supporting Information. The first module describes the cell shape in terms of the phase field method and is similar to our previous work. In this method, an auxiliary non-physical field, ϕ, is introduced to distinguish between the interior and exterior of the cell. The membrane is then modeled as a diffusive interface between these two values (here, $\phi = 1$ for the inside the cell and $\phi = 0$ for the outside). The main advantage of this method is that it avoids the need for explicit boundary tracking techniques. Consequently, it has been applied successfully to a large amount of free-boundary problems [30, 31, 32, 33, 22, 23]. In our case, the dynamic equation for the phase field is written as

$$\frac{\partial \phi}{\partial t} = -\mathbf{u} \cdot \nabla \phi + \Gamma(\epsilon \nabla^2 \phi - \frac{G'}{\epsilon} + c\epsilon|\nabla \phi|) \qquad [1]$$

where the advection term couples the phase field to the local actin flow velocity, $\mathbf{u}$, c denotes the local curvature, Γ is a Lagrangian multiplier, ϵ is the parameter controlling the width of the cell boundary, and G is a double well potential with minima at $\phi = 1$ and $\phi = 0$. This description is similar to the one we used previously except that we no longer enforce a constant cell area and that, following Ref. [33], we have added the last term to stabilize the phase field interface.

The second module describes the actin network which is treated as a viscous fluid [19] in the quasi steady approximation:

$$\nu_0 \nabla \cdot [\phi(\nabla \mathbf{u} + \nabla \mathbf{u}^T)] + \nabla \cdot \sigma_{\mathrm{myo}} + \nabla \cdot \sigma_{\mathrm{poly}} + \mathbf{F}_{\mathrm{mem}} + \mathbf{F}_{\mathrm{adh}} = \mathbf{0} \quad [2]$$

where ν_0 is the effective viscosity of actin network. Through explicit simulations, we have verified that solving the time-dependent equation for the actin flow does not lead to qualitatively different results. The first term represents the symmetrized strain rate tensor while the next two terms describe the contractile stress generated by myosin and the expansive stress due to actin filament polymerization, respectively, and are detailed in the Supporting Information [18]. The fourth term in this equation represents the membrane forces (surface tension and bending force) and are implemented in the phase field approach as before [34, 22].

The last term in the equation for the actin flow represents the forces due to the adhesion mechanism, described in the third module. It contains a spatially uniform drag force that is linearly proportional to the velocity of the cell. Additionally, we consider adhesive forces arising from discrete adhesion complexes. Newly created complexes are in the gripping mode and are modeled as springs with ends that are attached to the substrate and to the actin network. The position of the former is fixed in the laboratory frame of reference while the position of the latter is subject to movement due to actin flow. Hence, once the actin network starts to flow, these springs stretch and exert a force on both the actin network and the substrate. As the network continues to flow, the spring is stretched further and its probability of breaking increases. Once the adhesive bond is broken, the complexes operate in the slipping mode and the adhesive force is modeled as a simple drag force. Finally, the complexes disappear at a constant rate and when encountering the cell boundary, after which a new one is immediately created, keeping the number of adhesion sites fixed. The location of a new adhesion site is chosen from a probability distribution density that is proportional to the actin density. In a moving cell, this concentration is high near the leading edge and low near the trailing edge of the cell, leading to nascent adhesion sites that are concentrated at the front of the cell.

The final module in our model contains reaction-diffusion equations for the actin filament and myosin concentrations, ρ_a and ρ_m. The equation for actin contains an advection term, a diffusion term and a reaction kinetics term. We will present here results for a specific choice of the reaction kinetics but our model is equally applicable to different actin-myosin models. Our reaction term is a function $f(\rho_a, \rho_a^{\mathrm{cyt}})$ that also depends on the cytosolic actin monomer concentration ρ_a^{cyt}. Since actin monomer diffuse rapidly, we will assume that this monomer concentration is uniform. The mass-conserving function f is chosen to be bi-stable with solutions corresponding to small and large actin concentrations [35, 36]. Choosing the total actin concentration neither too large nor too small leads to a symmetry broken solution in which one part of the cell has a high actin concentration and the remainder has a small actin concentration. The equivalent equation for the conserved myosin concentration describes myosin advection due to actin and diffusion. This diffusion is assumed to be a function of actin such that the diffusion constant decreases for increasing actin concentration. These equations can be incorporated into the phase field model for a moving cell with zero-flux boundary conditions as has been described before [37, 22]:

$$\frac{\partial}{\partial t}(\phi \rho_a) = -\nabla \cdot (\phi \rho_a \mathbf{u}) + D_a \nabla \cdot (\phi \nabla \rho_a) + \phi f(\rho_a, \rho_a^{\mathrm{cyt}}) \qquad [3]$$

$$\frac{\partial}{\partial t}(\phi \rho_m) = -\nabla \cdot (\phi \rho_m \mathbf{u}) + D_m(\rho_a) \nabla \cdot (\phi \nabla \rho_m) \qquad [4]$$

where D_a and $D_m(\rho_a)$ are the diffusion coefficients of the two fields. Note that D_a does not represent physical diffusion but can be thought of as an effective diffusion constant arising from random events that include other actin related proteins and polymerization and depolymerization processes [38].

The partial differential equations [1-4] are solved on a 800×200 rectangle with grid size of $0.2\mu m$ and time step $\Delta t = 10^{-4} s$. To reduce computational costs we assumed perfect symmetry around the midline of the cell shown in Fig. 1B and only consider half of the cell. The force generated by each adhesion site is distributed equally to the nearest four grids that encloses the site. To reduce the computing time even further, we periodically shift our computation box such that the cell remains in the central portion of the box. The actin flow equation is solved using an implicit scheme and the reaction diffusion equations are calculated explicitly at locations where $\phi > 10^{-4}$. The parameters used in the simulations are provided in Supporting Table 1.

Results and Discussion

Steady state cell shapes. A typical simulation starts from a discoid cell with radius $r_0 = 10\mu m$ and with a uniform myosin density $[\rho_m^0]$. To break the symmetry and to determine the cell's direction, the initial actin filament concentration is chosen to be nonzero only in the front half of the cell. The ensuing polymerization of actin filaments pushes the cell forward, resulting in myosin being advected to the back of the cell. The increase of myosin at the back of the cell produces contractile stress and retracts the cell rear, resulting in cell motion. After a transitory period, the cell reaches a stationary fan-like shape, (Fig. 2A), and moves at constant speed. Fig. 2B and Fig. 2C show the corresponding steady state distribution of actin filaments and myosin, respectively.

Actin flow. The map of the actin flow produced by our model for the steady state shape corresponding to Fig. 2 is shown in Fig. 3A. Here, blue indicates retrograde flow, red corresponds to anterograde flow and the vectors correspond to the local actin flow velocity. As can be seen from these figures, the actin network flows forward in most parts of the cell with increasing speed near the back and the sides of the cell. However, the front part of the cell is characterized by a retrograde flow. This is further illustrated in Fig. 3D where we plot the actin flow velocity along the midline of the cell (shown as the dashed line in Fig.1B). The retrograde velocity along this line reaches a maximum magnitude of $\sim 0.012 \mu \mathrm{m/s}$. The sharp increase in flow velocity ahead of the retrograde flow zone represents the forward movement of the cell boundary, generated by the polymerization of actin filaments. At steady state, this forward velocity is identical

to the velocity of the back ($v_{\rm front} = v_{\rm back} = v_{\rm cell} = 0.14\mu{\rm m/s}$) as both boundaries move forward with the same speed.

Substrate stress. Fig. 3B illustrates the stress map of the substrate corresponding to the cell in A. Here, red represents forward, blue represents rearward stress and the arrows indicate the local stress magnitude and direction. The cell-to-substrate stress contains contributions from the basal level friction between the cell and the substrate, friction from the slipping sites and the stress from the gripping sites, mediated through stretched springs. The stress was computed assuming that the substrate is very rigid and that substrate deformations can be ignored. We have checked that the substrate stress, including the uniform drag force, sums up to zero at steady state, such that the net force on the cell vanishes. The stress map reveals that the stress is directed towards the back in roughly the front half of the cell and directed forward in the trailing part of the cell.

Actin stress alignment. To investigate the alignment between actin flow and substrate stress we computed the angle between the actin flow and the substrate stress, θ. A map of $\cos\theta$ is shown in Fig. 3C using a color scale with red corresponding to $\cos\theta = 1$ and blue corresponding to $\cos\theta = -1$. If adhesion were purely due to frictional drag, the substrate stress would always be in the same direction as the actin flow. Indeed, in most of the cell, the map reveals that the actin flow and substrate stress are aligned. At the central part of the cell, however, the stress is not perfectly aligned with the actin flow ($\cos\theta < 1$) and can even be opposite to the actin flow ($\cos\theta = -1$).

Distribution of adhesion sites. In Fig. 3E we show the time-averaged distribution of adhesion sites that are in the gripping mode while in 3F we plot the equivalent distribution for adhesion sites in the slipping mode. Clearly, most of the gripping sites are located in the front part of the cell, while the slipping sites are located at the back of the cell. Furthermore, due to their significant decay rate, most of these sites are found away from the trailing edge of the cell.

Role of myosin and adhesion on cell morphologies and flow patterns. Within our model, it is straightforward to investigate cell morphologies and flow patterns for different parameters, corresponding to experimental perturbations. We focus here on the effects of myosin contractility and adhesion strength. Experimentally, the former can be altered using blebbistatin (a myosin inhibitor) or calyculin A (a phosphatase inhibitor that activates myosin contraction) while the latter can be changed by coating the substrate with specific polymers [6]. The corresponding numerical parameters in our model are the total myosin concentration ρ_m and the gripping force parameter F^0_{grip}.

In Fig. 4 we plot the simulated cell morphologies for several different combinations of myosin concentration and adhesion strengths. The initial myosin density is varied from high (top row), to medium (middle row), and to low (bottom row) while the gripping strength increases from left to right. All the cell shapes shown in Fig. 4 are stationary except the one with the smallest myosin concentration and highest cell-substrate adhesion (right-bottom corner), which exhibits shape oscillations. For low gripping strength (left column), cells become rounder as the amount of myosin increases. In contrast, the morphologies of cells with intermediate or high gripping strength (middle and right column in Fig. 4) change in a more complicated fashion: cells with low and high myosin concentrations are rounder than cells with intermediate myosin concentrations.

Further quantification of the effects of varying myosin concentration and cell-substrate adhesion is presented in Fig. 5 where we plot several quantities as a function of the gripping force parameter F^0_{grip} (adhesion strength) for $\rho_m = 0.3\mu m^{-2}$ (dashed line, corresponding to the middle row in Fig. 4) and $\rho_m = 0.4\mu m^{-2}$ (solid line, upper row in Fig. 4). In Fig. 5A we plot the area of the cell as a function of the cell-substrate adhesion. This area is smaller for larger myosin concentrations and increases for increasing adhesive strengths. In Fig. 5B we report the maximum retrograde actin flow which is reduced for increasing gripping strength and decreasing myosin concentration. In Fig. 5C we plot the aspect ratio, defined as the ratio between the width and the length of the cell. The aspect ratio of cells with a large myosin concentration shows a monotonic increase in the aspect ratio as the gripping strength is increased. In contrast, the aspect ratio for an intermediate myosin concentration, corresponding to the middle row in Fig. 4, does not change monotonically with gripping strength: the aspect ratio is small for low and high values of F^0_{grip} and reaches a maximum for $F^0_{grip} = 5Pa$.

Comparison with experimental results. A comparison of the numerical results presented above with experimental data reveals that our model is able to capture most experimental findings. First of all, and consistent with our earlier work [22], the stationary shapes closely match the experimentally observed cell morphologies. A steadily moving cell for intermediate adhesion strength and myosin concentration exhibits a fan-like morphology (Fig. 2). Our results also compare favorably to the experimental data in the study of Barnhart *et al.* in which the myosin activity and adhesion strength was altered [6]. In particular, the morphologies shown in Fig. 4 are remarkably consistent with the ones reported in their experimental study. For example, the experiments also found that the area decreases for increasing myosin activity and increasing cell-substrate adhesion (compare with Fig. 5A). Furthermore, our numerically obtained aspect ratio for intermediate myosin concentrations (middle row in Fig. 4) also exhibits a biphasic dependence on adhesion strength, with cells crawling at intermediate adhesion strength displaying the highest aspect ratio (Fig. 5C).

Our actin and myosin distributions are consistent with experimental observations which show that actin is enriched at the front of the cell and myosin is concentrated in the back half of the cell [39, 2]. The actin flow pattern is in general accordance with the experimentally observed patterns which show a retrograde flow with a small velocity in the front of the cell and a larger anterograde flow at the cell rear [3, 39, 8, 2]. Also, the actin flow was reported to decrease for increased adhesion strengths, similar to our findings shown in Fig. 5B [6]. Finally, our stress map is qualitatively similar to the maps obtained in experiments using traction force microscopy [2]. In particular, as in the experiments, we observe that the region of rear-ward stress extends further away from the leading edge than the zone of retrograde actin flow. This can be seen in Fig. 3C which shows that the actin flow and stress direction are in opposite direction in the central part of the cell.

Motility mechanism. Taken together, our results suggest the following biophysical picture of cell movement: Cell movement is generated through the asymmetric distribution of actin filaments and myosin. The actin is concentrated at the front of the cell, leading to protrusive forces that push the membrane forward. Since myosin is attached to the actin filaments, it is advected with actin towards the rear of the cell. As a result of the bi-stable reaction kinetics (f in Eq. 3), the actin concentration is high in the front part of the cell and drops rapidly to a small value in the remainder of the cell, leading to an actin and myosin concentration profile as in Fig. 2B and C. The expansive stress from the actin network, together with the contractile stress of myosin, lead to retrograde flow in the front part of the cell as the network is both pushed (by actin) and pulled backwards (by myosin). At the rear of the cell, however, the actin must move with the cell's velocity and in the anterograde direction. The result is an actin velocity profile as in Fig. 3A and D.

Adhesion sites are formed with a probability distribution that is proportional to the actin concentration. Thus, new ones are predominantly formed near the front of the cell where they are in the gripping mode. Since the actin near the front of the cell flows in the retrograde direction, these sites will move backwards, resulting

in retrograde stress on the substrate (Fig. 3B). After their formation, these sites become more strongly attached to the substrate and are stretched further, increasing the retrograde cell-substrate stress. Once the actin flow reverses its direction from retrograde to anterograde, the length of the spring is reduced, leading to a decreasing rearward stress. Eventually, as the actin continues to flow in the anterograde direction, the adhesion springs are stretched in the forward direction, resulting in forward substrate stresses. Hence, as was observed in the experiments [2], the location where retrograde flow switches to anterograde flow does not coincide with the location where the stress changes from forward to rearward, resulting in an opposite alignment of actin flow and substrate stress in the central part of the cell (Fig. 3C). Specifically, the region of opposite alignment corresponds to the part of the cell in which the actin flow is anterograde while the adhesion spring is still stretched in the rearward direction. Since the flow velocity is roughly linear (Fig. 3D), the amount of time to return from the maximal rearward extension to the unstretched position is roughly identical to the amount of time during which the spring is being stretched backwards. Hence, the spatial extent of the region in which the stress and flow are aligned oppositely is roughly identical to the spatial extent of the frontal region where the flow and substrate stress are aligned. As the anterograde flow magnitude increases, the adhesion force increases until the adhesive bond is broken. This is also shown in Fig. 5D where we plot the average substrate stress along the midline of the cell where negative values correspond to rearward stress and positive values correspond to forward stress. This figure demonstrates that the anterograde flow increases the forward substrate stress rapidly, after which the bonds break. Once broken, these adhesive sites exert a forward stress due to frictional drag (Fig. 3E and F).

Our parameter modifications show that the cell morphology, along with actin flow speeds, depend not only on cell-substrate adhesion but also on myosin activity (Fig. 4 and 5). For low gripping strengths (left column in Fig. 4), increasing the myosin concentration results in increased contractility and, hence, rounder cells with a smaller aspect ratio (Fig. 5A). Increasing the gripping strength leads to a transition from gripping to slipping adhesion sites that occurs at a larger cell-substrate stress. Consequently, as can be seen most clearly in the bottom row of Fig. 4, cells become more elongated in the direction of their motion.

Summary and possible extensions. Even though our model results are consistent with experimental studies, it has several limitations and can be extended in various ways. For example, our cell is treated as a two-dimensional object. This is a reasonable approximation for the lamellipodium but is not sufficient to describe the bulbous cell body. Extension to three dimensions [29] are in principle straightforward albeit computationally more intensive. Also, we have focused here on solutions that are symmetric around the midline of the cell (dashed line in Fig. 1B). Hence, any left-right asymmetries or bipedal locomotion as reported in the literature [40, 6] can not be captured in our numerical study. A numerical extension that solves the complete cell shape is straightforward. Note, however, that the mechanisms underlying the observed left-right asymmetry are not precisely known and might not be present in the current model. In addition, unlike our numerical studies, experiments show a significant increase in adhesion at the sides of the cell. This suggests a specific mechanism, absent in our model, that is responsible for this accumulated adhesion at the sides of the cell. Furthermore, it would be interesting to explore the dependence of cell velocity on model parameters and substrate properties. We have found that the cell speed depends non-monotonically of F_{grip}, with lower speeds at high and low adhesion strength (data not shown). This peak in cell speed appears to depend on the myosin concentration and a further exploration is warranted. Also, in our model the cell morphology is treated deterministically and is not able to address experimental results which show cell shapes with a noisy periphery under low myosin activity and higher adhesion strength conditions [6]. Furthermore, our reaction-diffusion model can be extended to include more complicated actin-myosin dynamics. For example, it has been suggested that myosin might disassemble F-actin near the cell back [8]. In addition, it would be interesting to include extra pathways to control ρ_a^{tot}, ensuring that the cell is able to polarize [35]. Also, we have assumed that the substrate is infinitely rigid. Experiments have shown that substrate rigidity can affect the shapes and motility properties of cells [24], and our previous work has shown how to describe substrate deformations [26]. Finally, it would be worth exploring the effects of barriers on the cell velocity, as was investigated in recent experiments [41]. We believe that our model is well-suited to start exploring these extensions, which should lead to a more fundamental biophysical understanding of cell motility.

In summary, we have presented a computational model for cell motility that incorporates cytosolic actin flow, discrete adhesion sites, myosin contraction, actin polymerization, and membrane forces. Our computational methodology employs a phase-field, enabling an efficient determination of the morphology of the cell. The results of our model are in good agreement with experimental data. In particular, it is able to reproduce maps of actin flow, substrate stress and their alignment as observed in recent experiments that combined traction force microscopy and actin flow measurements. Our results suggest that cell motion and its associated cell morphology and actin flow patterns are controlled by the collective effects of myosin contraction, actin polymerization, and adhesion site dynamics.

ACKNOWLEDGMENTS. This work was supported by NIH Grant P01 GM078586.

1. Pollard, T. D. & Borisy, G. G. Cellular motility driven by assembly and disassembly of actin filaments. *Cell* 112, 453–455 (2003).
2. Fournier, M. F., Sauser, R., Ambrosi, D., Meister, J. J. & Verkhovsky, A. B. Force transmission in migrating cells. *J Cell Biol* 188, 287–297 (2010).
3. Jurado, C., Haserick, J. R. & Lee, J. Slipping or gripping? Fluorescent speckle microscopy in fish keratocytes reveals two different mechanisms for generating a retrograde flow of actin. *Mol Biol Cell* 16, 507–518 (2005).
4. Cramer, L. P. Molecular mechanism of actin-dependent retrograde flow in lamellipodia of motile cells. *Front Biosci* 2, d260–d270 (1997).
5. Vallotton, P., Danuser, G., Bohnet, S., Meister, J. J. & Verkhovsky, A. B. Tracking retrograde flow in keratocytes: news from the front. *Mol. Biol. Cell* 16, 1223–1231 (2005).
6. Barnhart, E. L., Lee, K. C., Keren, K., Mogilner, A. & Theriot, J. A. An adhesion-dependent switch between mechanisms that determine motile cell shape. *PLoS Biol.* 9, e1001059 (2011).
7. Verkhovsky, A. B., Svitkina, T. M. & Borisy, G. G. Self-polarization and directional motility of cytoplasm. *Curr Biol* 9, 11–20 (1999).
8. Wilson, C. A. *et al.* Myosin II contributes to cell-scale actin network treadmilling through network disassembly. *Nature* 465, 373–377 (2010).
9. Jockusch, B. M. *et al.* The molecular architecture of focal adhesions. *Annu. Rev. Cell Dev. Biol.* 11, 379–416 (1995).
10. Gardel, M. L., Schneider, I. C., Aratyn-Schaus, Y. & Waterman, C. M. Mechanical integration of actin and adhesion dynamics in cell migration. *Annu Rev Cell Dev Biol* (2010).
11. Anderson, K. I. & Cross, R. Contact dynamics during keratocyte motility. *Curr. Biol.* 10, 253–260 (2000).
12. Choi, C. K. *et al.* Actin and alpha-actinin orchestrate the assembly and maturation of nascent adhesions in a myosin II motor-independent manner. *Nat. Cell Biol.* 10, 1039–1050 (2008).
13. Mitchison, T. & Kirschner, M. Cytoskeletal dynamics and nerve growth. *Neuron* 1, 761–772 (1988).
14. Heidemann, S. R. & Buxbaum, R. E. Cell crawling: first the motor, now the transmission. *J Cell Biol* 141, 1–4 (1998).
15. Smilenov, L. B., Mikhailov, A., Pelham, R. J., Marcantonio, E. E. & Gundersen, G. G. Focal adhesion motility revealed in stationary fibroblasts. *Science* 286, 1172–1174 (1999).
16. Gracheva, M. E. & Othmer, H. G. A continuum model of motility in ameboid cells. *Bull. Math. Biol.* 66, 167 – 193 (2004).
17. Larripa, K. & Mogilner, A. Transport of a 1D viscoelastic actin-myosin strip of gel as a model of a crawling cell. *Phys. A* 372, 113 (2006).
18. Carlsson, A. E. Mechanisms of Cell Propulsion by Active Stresses. *New J Phys* 13 (2011).

19. Rubinstein, B., Fournier, M. F., Jacobson, K., Verkhovsky, A. B. & Mogilner, A. Actin-myosin viscoelastic flow in the keratocyte lamellipod. *Biophys J* 97, 1853–1863 (2009).
20. Wolgemuth, C. W., Stajic, J. & Mogilner, A. Redundant mechanisms for stable cell locomotion revealed by minimal models. *Biophys. J.* 101, 545–553 (2011).
21. Yang, L. *et al.* Modeling cellular deformations using the level set formalism. *BMC Syst Biol* 2, 68 (2008).
22. Shao, D., Rappel, W.-J. & Levine, H. Computational model for cell morphodynamics. *Phys Rev Lett* 105, 108104 (2010).
23. Ziebert, F., Swaminathan, S. & Aranson, I. S. Model for self-polarization and motility of keratocyte fragments. *J R Soc Interface* (2011).
24. Chan, C. E. & Odde, D. J. Traction dynamics of filopodia on compliant substrates. *Science* 322, 1687–1691 (2008).
25. Cirit, M. *et al.* Stochastic model of integrin-mediated signaling and adhesion dynamics at the leading edges of migrating cells. *PLoS Comput Biol* 6, e1000688 (2010).
26. Buenemann, M., Levine, H., Rappel, W. J. & Sander, L. M. The role of cell contraction and adhesion in dictyostelium motility. *Biophys J* 99, 50–58 (2010).
27. Enculescu, M., Sabouri-Ghomi, M., Danuser, G. & Falcke, M. Modeling of protrusion phenotypes driven by the actin-membrane interaction. *Biophys J* 98, 1571–1581 (2010).
28. Zimmermann, J., Enculescu, M. & Falcke, M. Leading-edge-gel coupling in lamellipodium motion. *Phys Rev E Stat Nonlin Soft Matter Phys* 82, 051925 (2010).
29. Herant, M. & Dembo, M. Form and function in cell motility: from fibroblasts to keratocytes. *Biophys J* 98, 1408–1417 (2010).
30. Karma, A. & Rappel, W.-J. Quantitative phase-field modeling of dendritic growth in two and three dimensions. *Phys. Rev. E* 57 (1998).
31. Folch, R., Casademunt, J., Hernandez-Machado, A. & Ramirez-Piscina, L. Phase-field model for Hele-Shaw flows with arbitrary viscosity contrast. I. Theoretical approach. *Phys Rev E* 60, 1724–33 (1999).
32. Karma, A., Kessler, D. A. & Levine, H. Phase-field model of mode III dynamic fracture. *Phys Rev Lett* 87, 045501 (2001).
33. Biben, T., Kassner, K. & Misbah, C. Phase-field approach to three-dimensional vesicle dynamics. *Phys Rev E Stat Nonlin Soft Matter Phys* 72, 041921 (2005).
34. Du, Q., Liu, C. & Wang, X. Simulating the deformation of vesicle membranes under elastic bending energy in three dimensions. *J Comp Phys* 212, 757–777 (2006).
35. Otsuji, M. *et al.* A mass conserved reaction-diffusion system captures properties of cell polarity. *PLoS Comput. Biol.* 3, e108 (2007).
36. Mori, Y., Jilkine, A. & Edelstein-Keshet, L. Wave-pinning and cell polarity from a bistable reaction-diffusion system. *Biophys J* (2008).
37. Kockelkoren, J., Levine, H. & Rappel, W. J. Computational approach for modeling intra- and extracellular dynamics. *Phys Rev E* 68, 037702 (2003).
38. Carlsson, A. E. Dendritic actin filament nucleation causes traveling waves and patches. *Phys Rev Lett* 104, 228102–228102 (2010).
39. Schaub, S., Bohnet, S., Laurent, V. M., Meister, J. J. & Verkhovsky, A. B. Comparative maps of motion and assembly of filamentous actin and myosin II in migrating cells. *Mol. Biol. Cell* 18, 3723–3732 (2007).
40. Barnhart, E. L., Allen, G. M., Julicher, F. & Theriot, J. A. Bipedal locomotion in crawling cells. *Biophys. J.* 98, 933–942 (2010).
41. Heinemann, F., Doschke, H. & Radmacher, M. Keratocyte lamellipodial protrusion is characterized by a concave force-velocity relation. *Biophys. J.* 100, 1420–1427 (2011).

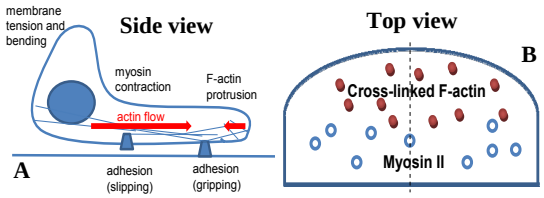

Fig. 1. (A) Schematic side view of a migrating cell. Our model describes the thin lamellipodium extending in front of the bulbous cell body and is approximated as a two-dimensional sheet, shown in the top view of (B). Within this lamellipodium, cross-linked actin, responsible for protrusion, is concentrated at the front while myosin, generating contraction, is mainly found at the back of the cell. Forces are transmitted to the substrate via discrete adhesion sites that can either be in the gripping mode (schematically shown in red) or in the slipping mode (schematically shown in blue). As a result, the actin network exhibits a small retrograde flow in the front part of the cell and a anterograde flow in the back half of the cell. The midline of the cell, shown as a dashed line in (B), is assumed to be a line of symmetry, facilitating the computations.

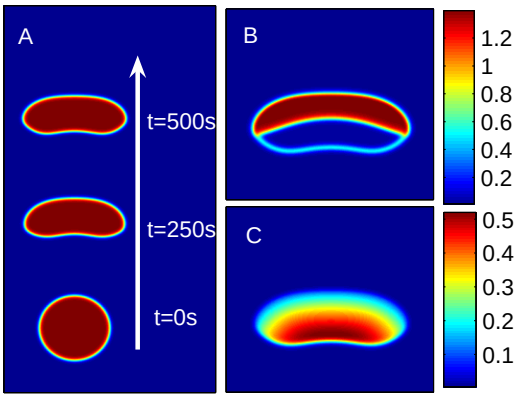

Fig. 2. Snapshots of cell migration. (A) Three successive snapshots of a typical simulation of a cell evolving and reaching a stationary shape with aspect ratio $S = 2.6$ and speed $v = 0.14\mu m/s$. The corresponding steady-state distributions of F-actin and bound myosin are shown in (B) and (C), respectively, representing a a 40μm$\times$40μm area. Parameters are given in Supporting Table 1 with $F^0_{grip} = 5\mathrm{Pa}$ and $[\rho^0_m] = 0.3\mu\mathrm{m}^{-2}$.

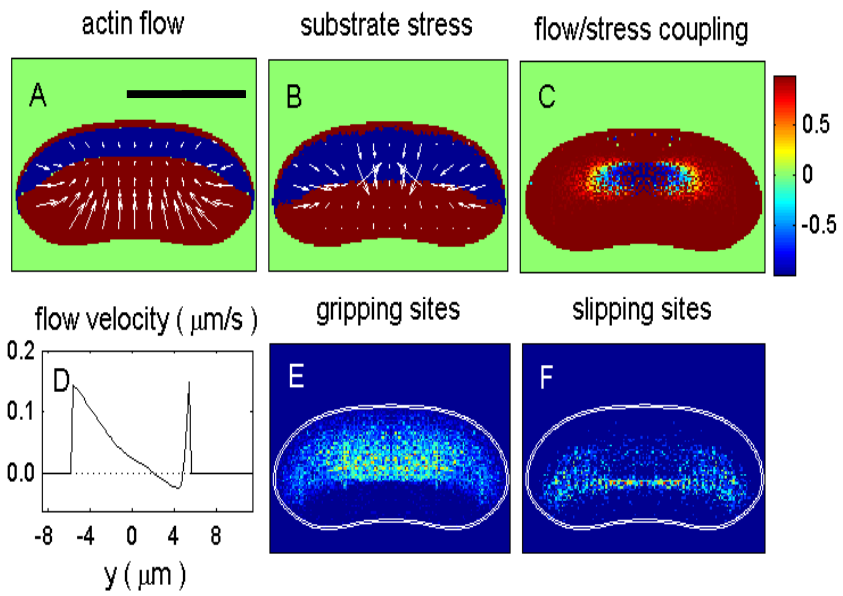

Fig. 3. Steady-state maps of actin flow and substrate stress. Maps of actin flow (A), substrate stress (B), gripping sites (E) and slipping sites (F) corresponding to the cell morphology in Fig. 2. (C): Coupling between actin flow and stress, measured by computing the cosine of the angle between flow vector and stress vector. (D): Actin flow velocity along the midline of the cell. The actin flow velocity equals the cell's speed (0.14 μm/s) at the back of the cell and, due to the phase-field implementation, at the front of the cell. The scale bar corresponds to 10μm.

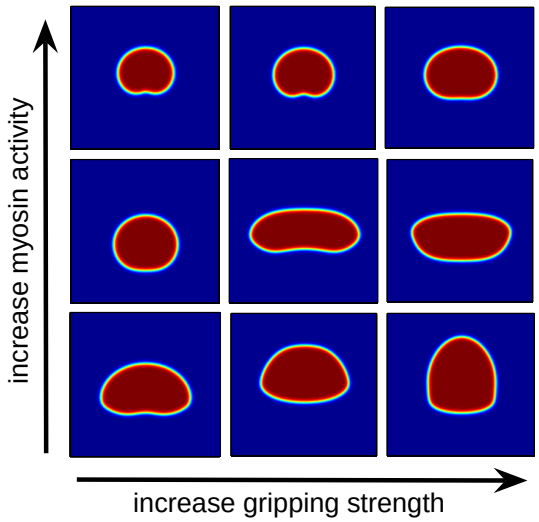

Fig. 4. Morphologies for different cell-substrate adhesion and myosin concentration values, shown in 40μm$\times$40μm plots. The gripping strength is tuned by F^0_{grip}: $F^0_{grip} = 1\mathrm{Pa}$ (left column), $F^0_{grip} = 5\mathrm{Pa}$ (middle column) and $F^0_{grip} = 10\mathrm{Pa}$ (right column). The myosin concentration varies from $[\rho^0_m] = 0.2\mu\mathrm{m}^{-2}$ (bottom row) to $[\rho^0_m] = 0.3\mu\mathrm{m}^{-2}$ (middle row) and $[\rho^0_m] = 0.4\mu\mathrm{m}^{-2}$ (top row). Other parameters are as in previous figures.

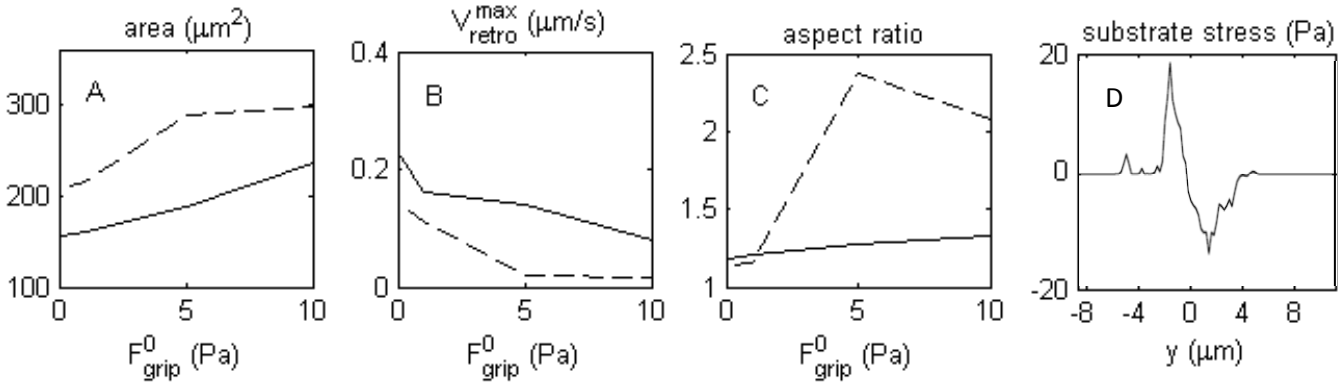

Fig. 5. Quantification of the effects of different gripping strengths and myosin concentrations. Solid lines represent $[\rho_m^0] = 0.4\mu\mathrm{m}^{-2}$ and dashed lines correspond to $[\rho_m^0] = 0.3\mu\mathrm{m}^{-2}$. Plotted as a function of the gripping strength are the cell area (A), maximum retrograde velocity (B), and aspect ratio (C). (D): The average substrate stress along the midline of the cell.